

Cloudiness and Marine Boundary Layer Dynamics in the ASTEX Lagrangian Experiments. Part II: Cloudiness, Drizzle, Surface Fluxes, and Entrainment

CHRISTOPHER S. BRETHERTON

Atmospheric Science Department, University of Washington, Seattle, Washington

PHILIP AUSTIN

Atmospheric Sciences Programme, University of British Columbia, Vancouver, British Columbia, Canada

STEVEN T. SIEMS

Monash University, Clayton, Victoria, Australia

(Manuscript received 26 June 1994, in final form 3 January 1995)

ABSTRACT

The Analysis of the Atlantic Stratocumulus Transition Experiment (ASTEX) Lagrangians started in Part I is continued, presenting measurements of sea surface temperature, surface latent and sensible heat fluxes from bulk aerodynamic formulas, cloud fraction, and drizzle rate for the two Lagrangians, mainly using data from horizontal legs flown by the Electra and C130. Substantial drizzle, averaging 1 mm day^{-1} at the surface, was measured during the first Lagrangian. The surface fluxes increased rapidly as the air mass advected over rapidly increasing SST. Cloud fraction remained high throughout. During the second Lagrangian, drizzle formed in the stratocumulus layer but mainly evaporated in the deep, dry cumulus layer and the subcloud layer before reaching the surface. Stratocumulus cloud cover was thickest when moist air lay above the inversion and then it dissipated to leave only cumuli once dry air advected over the inversion.

Three methods are compared for determining entrainment rate (European Centre for Medium-Range Weather Forecasts analyses of mean vertical motion, calculation of a water budget, and the ozone flux-jump method). While all three methods have significant uncertainties, their predictions are all consistent with an entrainment rate of $0.7 \pm 0.3 \text{ cm s}^{-1}$ for the first Lagrangian and $0.6 \pm 0.3 \text{ cm s}^{-1}$ for the second Lagrangian. Corresponding estimates of the time-dependent horizontal divergence are also presented.

Estimates of the cumulus mass flux, internal mixing time, and entrainment dilution time for the boundary layers observed during the two Lagrangians are also presented.

1. Introduction

This paper continues the analysis of the Atlantic Stratocumulus Transition Experiment (ASTEX) Lagrangian Intensive Observing Periods (IOPs) in Bretherton and Pincus (1994, hereafter Part I), to which the reader is referred for an overall discussion of the Lagrangian IOPs. Together with Part I, these observations provide all necessary boundary conditions and a variety of verification data for comparisons with large-eddy simulation, turbulence closure models, and bulk parameterizations of the cloud-topped marine boundary layer (MBL). The estimation of the entrainment rate is a key component of chemical or thermodynamic budget studies of the MBL.

Section 2 uses data from the level Electra flight legs to determine sea surface temperature (SST), surface latent and sensible heat fluxes, cloud fraction, and drizzle rate for the two Lagrangian IOPs (which we call L1 and L2). In section 3, we compare three methods for determining the mean entrainment rate into the MBL, an important quantity for budget calculations and model comparisons that could not be directly measured. In section 4, we use the measurements of sections 2 and 3 to estimate timescales for internal mixing and for dilution of boundary layer air by entrainment. Section 5 presents the conclusions.

2. Data from the horizontal aircraft legs

Several fields, including SST, surface pressure, air-sea temperature difference, cloudiness, and drizzle, were derived from statistics from the horizontal aircraft legs and other sources.

Corresponding author address: Christopher S. Bretherton, Atmospheric Science Department, Box 351640, University of Washington, Seattle, WA 98195.

a. Sea surface temperature

Because of the paramount importance of accurate SSTs for determination of heat and moisture fluxes, four sources of SST data were compared. The Electra measured surface temperature with a downward-pointing Barnes PRT5 narrowband radiometer. A similar Barnes PRT4 radiometer was flown on the C130. For both Lagrangian IOPs we have compiled the horizontal average SST inferred from the lowest leg of all stacks flown by both aircraft. The Electra radiometer was calibrated before and after each flight, but the absolute calibration is accurate only to a few tenths of a kelvin, and the radiometer measurements can drift slightly during a flight. The C130 radiometer was calibrated only during L1. The R/V *Oceanus* took SST measurements as it followed the trajectory taken by the air column under study. During L1, only the first half of the Lagrangian trajectory was followed, because beyond that point the trajectory was rather uncertain. During the entirety of L2, the R/V *Oceanus* followed closely behind the air column. No research quality SST measurements were taken on the R/V *Oceanus* during ASTEX, so only a routine lower quality SST measurement was available. The water in the intake pipe for this SST measurement appears to have been somewhat warmed as it passed around the engine, biasing the measurements. A fourth source of SST data was a European Centre for Medium-Range Weather Forecasts (ECMWF) analysis, a smoothed blend of ship and satellite observations that is updated daily.

The ECMWF analyses do not resolve regions of large SST gradient or fine structure, such as the Azores Current, which flows along a sinuous east–west oceanic front just south of the Azores Islands and over which the L1 trajectory passed. However, since the ECMWF analyses involve many independent sensors, we assumed that averaged over each Lagrangian IOP the ECMWF analyses should be unbiased. We used this assumption to calculate and subtract out a mean bias for the R/V *Oceanus* SST measurements. We then used corrected and smoothed R/V *Oceanus* SSTs (or ECMWF for the latter part of L1) to determine nominal mean biases for each of the aircraft flights (Table 1). Figure 1 shows the corrected SST measurements taken during the two Lagrangian IOPs, along with a smoothed “best-guess” SST derived by drawing a smooth curve through the corrected R/V *Oceanus* and aircraft measurements that filters out temporal variability on scales of less than six hours. The corrections made to the aircraft and R/V *Oceanus* SSTs ensure that they are approximately equal. The smoothing in the ECMWF SST analysis is evident. Especially notable is the 4 K jump in SST experienced by the moving air mass during L1 in less than 24 hours as it crossed the Azores Current. The R/V *Oceanus* SST in L2 shows some oscillatory fine structure but steadily increases at an average rate of 1.7 K day⁻¹ from day 19 to 20.5.

TABLE 1. Inferred SST biases.

Platform	Flight	Time (days)	Bias (K)
R/V <i>Oceanus</i>	L1 and L2		1.0
Electra	RF05 (L1)	12.7–12.9	-0.4
	RF06 (L1)	13.2–13.4	-0.4
	RF07 (L1)	13.7–13.9	-0.4
	RF11 (L2)	18.9–19.1	-0.4
	RF12 (L2)	19.4–19.6	-0.8
	RF13 (L2)	19.9–20.1	-0.6
C130	RF14 (L2)	20.4–20.6	-0.6
	A209 (L1)	13.0–13.2	-0.4
	A210 (L1)	14.4–14.7	0.0
	A213 (L2)	19.2–19.4	0.0
	A214 (L2)	20.3–20.5	-1.5

b. Surface pressure, surface temperature, and surface fluxes

Using average values from the lowest leg of each Electra stack (which varied in height between 30 and 165 m), surface pressure and temperature were calculated (Fig. 2). Surface pressure was inferred hydrostatically from leg mean pressure and radar altimeter height, while surface temperature was calculated from leg mean temperature by assuming a dry adiabat between the surface and the leg height. The pressure slowly decreased as surface drag forced the air mass across the isobars. In both L1 and L2 the pressure decreases were on the order of 1–2 hPa. The observed pressures were in good agreement with the ECMWF analyses (not shown).

As seen in Fig. 2, in L1 the air minus sea temperature difference (using the best-guess SST) was initially 1 K, changing to -1 K as the air parcel moved over much warmer water. Since the air mass had been moving westward from warmer to colder water before reaching the R/V *Oceanus*, the initially positive air–sea temperature difference is plausible. In L2, the air–sea temperature difference was -0.2 to -0.5 K throughout, typical for an MBL advecting slowly toward warmer water. The air–sea temperature difference is a useful check on our best-guess SST; it would be hard to reconcile the observed cold advection with a positive air–sea temperature difference throughout L2 (as we would deduce if we regarded the aircraft SSTs as unbiased). Conversely, uncertainties in SST also render the exact size of the air–sea temperature difference somewhat uncertain.

From these SSTs and the surface temperature and mixing ratio and winds inferred from lowest-leg averages, bulk formulas were used to infer the heat and moisture flux (Fig. 3). A bulk transfer coefficient of $C_T = (.75 + .067 V) \times 10^{-3}$ was used, where V is the lowest-leg mean wind speed (Garratt 1977), with a constant offset of -0.2×10^{-3} to correct for the aircraft measurements being at 30 m or more above the surface

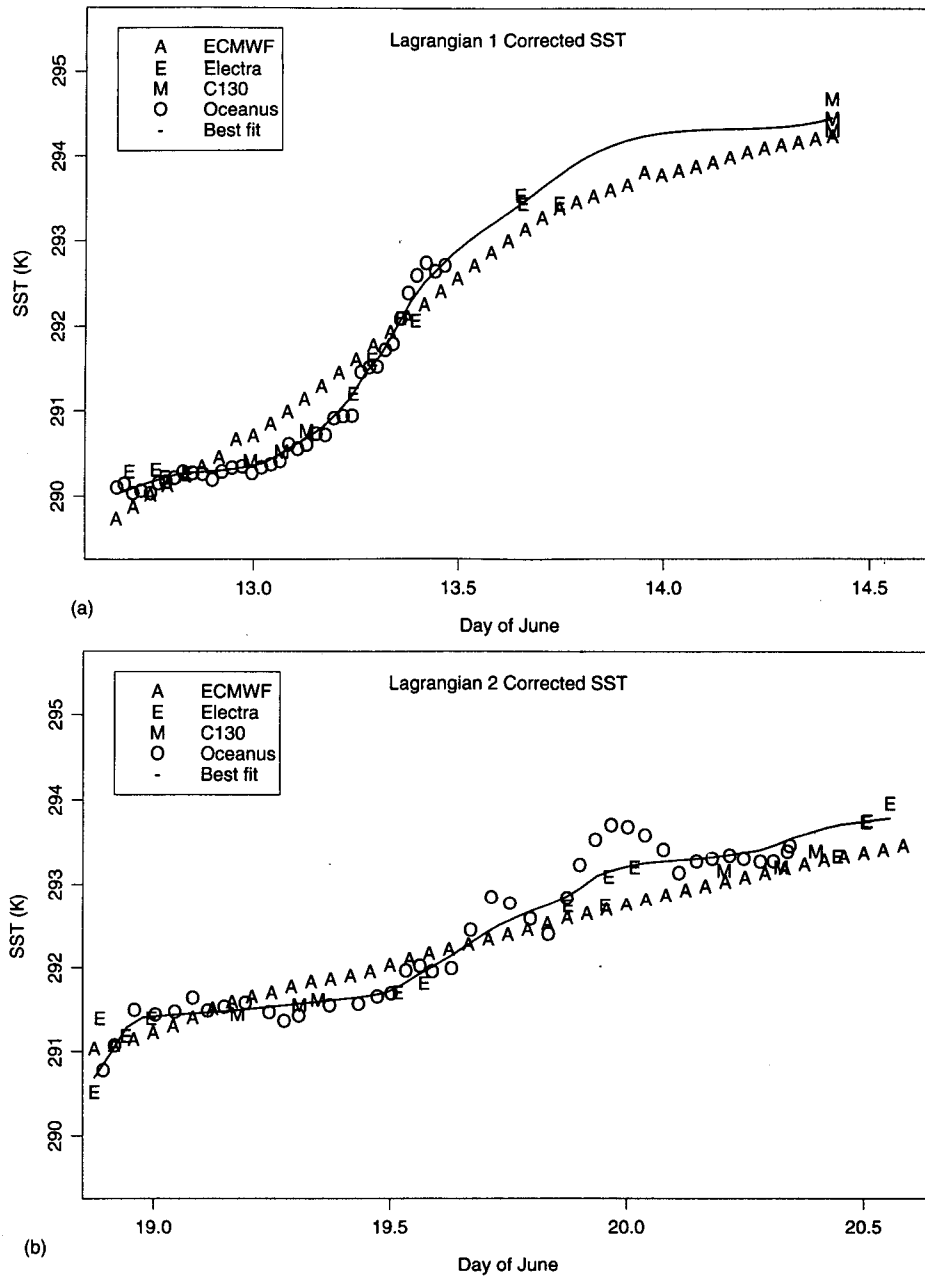


FIG. 1. Corrected SST measurements taken during the two Lagrangians.

rather than at 10 m. This offset was found by assuming a surface logarithmic layer between 10 m and a nominal flight level of 30 m using a surface roughness of $z_0 = 10^{-4}$ at a wind speed of $V_0 = 7 \text{ m s}^{-1}$ consistent with Charnock's formula (Stull 1988, pp. 265–266). The offset was then derived substituting these characteristic values into the formula

$$C_T(30 \text{ m}, V_0) - C_T(10 \text{ m}, V_0) = C_T(10 \text{ m}, V_0) \times [\{ \log(10/z_0) / \log(30/z_0) \}^2 - 1]. \quad (1)$$

Sensible heat fluxes ranged from -15 to $+15 \text{ W m}^{-2}$ in L1 and were typically 5 W m^{-2} in L2. Latent heat fluxes were initially quite small in L1 but rose to nearly 150 W m^{-2} on the warm side of the Azores Current. In L2, wind speed was lower but the MBL was relatively dry, so $100\text{--}150 \text{ W m}^{-2}$ latent heat fluxes were again seen.

c. Cloudiness

Two aircraft-based measures of cloudiness were compared. The first measure was cloud fraction en-

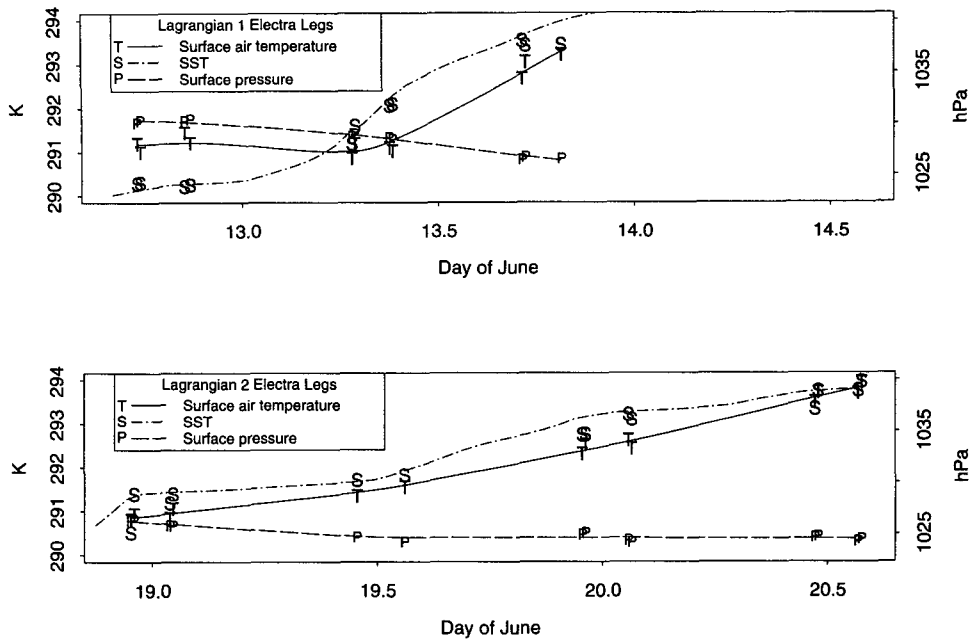


FIG. 2. Surface pressure and temperature inferred from Electra lowest-leg averages, and the best-fit SST from Fig. 1. Letters indicate measurements, and lines are best-fit curves.

countered on flight legs less than 30 hPa below the inversion, where stratocumulus cloud was concentrated if it was present. Each 1-s measurement was assumed to be in cloud if the Forward-Scattering Spectrometer Probe (FSSP) droplet concentration was greater than

10 cm^{-3} . A second radiometric measure of cloudiness was derived from the lowest-leg data using the upward-pointing Barnes PRT5 aboard the Electra, which measures in a narrow wavelength band in the water vapor window and hence is sensitive only to liquid water and

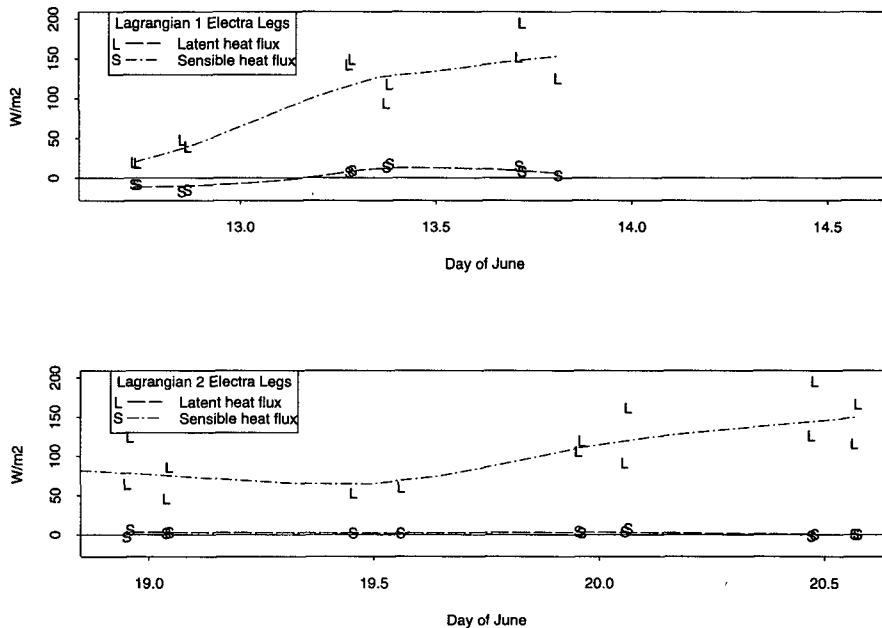


FIG. 3. Heat and moisture fluxes derived using bulk formulas from lowest-leg Electra measurements. Letters indicate measurements, and lines are best-fit curves.

not water vapor. Cloudiness was inferred whenever the brightness temperature exceeded 276 K. This threshold included all clouds with bases below 2 km (if we assume an SST of at least 290 K and a lapse rate of 7 K km⁻¹) but not high clouds or downgoing radiation due to weak water vapor emissions in the sampled wavelengths. The cloud fractions were insensitive to small (± 1 K) changes in the threshold. The C130 carried an upward-pointing PRT4 radiometer. However, we could not find a satisfactory threshold test for cloud using the PRT4 data, since the PRT4 is more sensitive than the PRT5 to water vapor emissions.

Results from the two methods and the satellite retrievals of Part I are compared for both Lagrangian IOPs in Fig. 4. The FSSP cloud fractions were higher by 10%–20% on average, though there is significant scatter. Hints of a diurnal cycle in cloudiness with a maximum around 0600–0800 local time are apparent for L2.

The in-cloud legs also give reliable estimates of the cloud droplet concentration N . For in-cloud legs with 30% or higher cloudiness, we estimated N as the leg-average FSSP droplet concentration (averaged over both cloudy and clear parts of the legs) divided by the FSSP-deduced cloud fraction. Consistent with the soundings presented in Part I, N was 50–150 cm⁻³, with a mean of 100 cm⁻³, in L1 and 150–275 cm⁻³, with a mean of 210 cm⁻³, in L2 (Fig. 5).

d. Drizzle

Precipitation was examined using a Particle Measurement Systems (PMS) 260X probe in the Electra

and a PMS 2D cloud probe on the C130. The 260X measures concentrations of droplets in 58 size bins ranging from radii of 20 to 310 μm , while the 2D-C's 32 bins range from 6.25 to 406.25 μm . We defined the drizzle rate to be the vertical droplet sedimentation flux found by assigning a radius-dependent fall speed (Beard 1976) to droplets in each size bin and summing over all bins. We defined the drizzle frequency to be the fraction of 20-s time intervals with an average rain rate greater than 1 mm day⁻¹. The leg-average drizzle rates and drizzle frequencies are plotted in Fig. 6 for L1 and in Fig. 7 for L2. The Electra and C130 drizzle rates may have systematic (and different) biases but this is difficult to assess from Figs. 6 and 7, since the rain rates were extremely variable. At the C130–Electra transition at day 13.2 of L1, an apparent fourfold increase in drizzle and twofold increase in drizzle fraction is seen, but at a similar transition at day 19.45 of L2 there is a large decrease in drizzle rate and fraction. In this paper we will accept drizzle measurements from both platforms at face value.

During days 12.8–13.8 during L1, drizzle reaching the surface was frequent, with drizzle found on all near-surface legs (pressure above 1000 hPa) between 9% and 54% of the time. A surface drizzle rate of 2.7 mm day⁻¹ was found at 13.4 days, and the mean drizzle rate over this period seems to have been about 1 mm day⁻¹. Even higher drizzle frequencies (up to 92%) and drizzle rates (up to 5.5 mm day⁻¹) were found in the cloud layer.

During the C130 flight on 14 June the 2D cloud probe measured concentrations of 25 μm droplets that

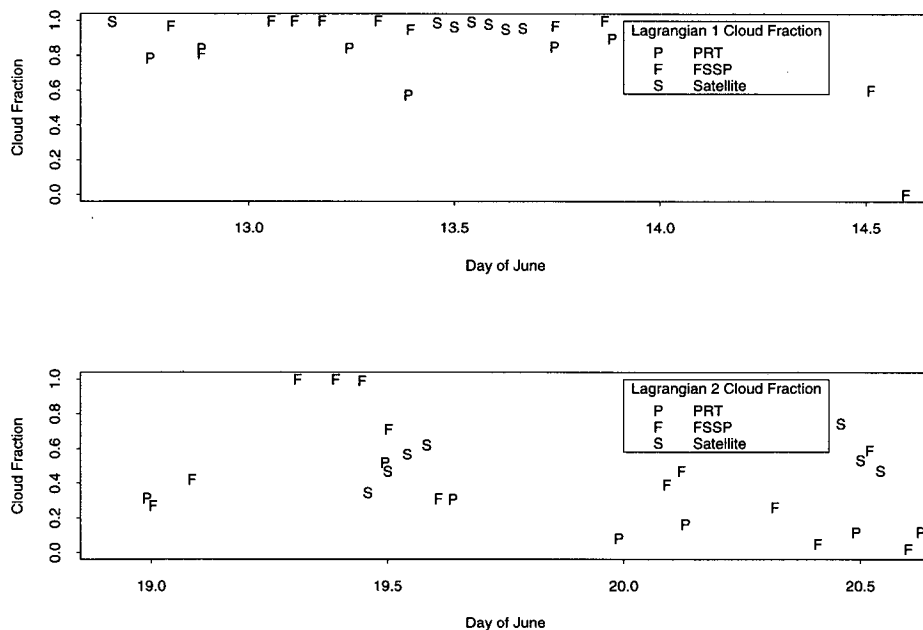


FIG. 4. Aircraft-derived cloud fraction from FSSP and upward pointing radiometer (PRT) measurements. Satellite-derived cloud fraction from Fig. 10 of Part I is also plotted for comparison.

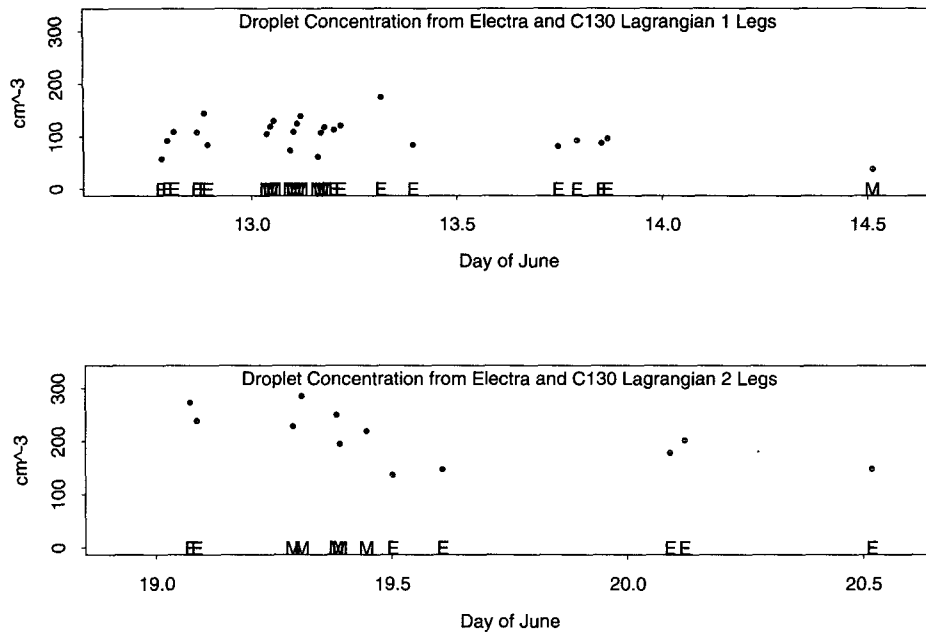


FIG. 5. Cloud droplet concentration from horizontal legs with cloud fraction greater than 30%. Letters E (Electra) and M (C130) at the base of the plot indicate the data-taking aircraft.

were 100–1000 times as large as simultaneous measurements from the C130 FSSP. An apparent explanation for the discrepancies is that a rain cover had been left off the probe the previous night (G. Martin 1993, personal communication). In accordance with the FSSP measurements, the drizzle rates and frequencies from this flight have been zeroed in Fig. 6.

During L2, very little precipitation appears to have reached the ground. Precipitation was recorded on only 3 of the 16 near-surface legs, and only on one of those legs in which the Electra flew through a convective rain shower (day 19.9) did the precipitation rate significantly exceed 0.1 mm day^{-1} . From day 19 to day 19.6, when the MBL was topped by a solid 100–500-m-thick stratocumulus layer, precipitation was forming aloft. Drizzle frequencies of 10%–90% and drizzle rates of 1–2 mm day^{-1} in the 50 hPa below the inversion base typify this period. The high drizzle frequency suggests that the precipitation was not falling out as cumulus showers but was forming mainly in the broad stratiform anvils detrained by the cumulus clouds. The much smaller drizzle rates at lower heights imply that almost all of this drizzle evaporated in the relatively deep and dry MBL, contributing to evaporative cooling in the cumulus and subcloud layers. Thus, the lack of precipitation at the surface is due not only to the suppression of drizzle formation in a dirtier air mass but also to the depth and dryness of the MBL.

3. Entrainment

An attractive feature of the Lagrangian strategy is that by removing horizontal advective contributions it

simplifies budgets of heat, moisture, and chemical species. However, one key unknown remains unmeasured—the entrainment rate. In this section, we present results from three different approaches to estimating entrainment rate:

- 1) ECMWF synoptic-scale analyses of vertical motion, coupled with the observed rate of change of inversion height following the MBL air column;
- 2) calculation of entrainment drying as a residual in the water budget of the MBL air column; and
- 3) inference of entrainment rate from ozone fluxes measured just below the entrainment interface and ozone jumps across the inversion.

The first two of these methods require a Lagrangian dataset, while the third does not.

a. ECMWF analyses of mean vertical motion

ECMWF operational analyses were archived for 0000, 0600, 1200, and 1800 UTC for every day of AS-TEX. Since the instantaneous ω (vertical pressure velocity) field from an analysis can be notoriously noisy, the following strategy was used to obtain a more representative ω field. From each analysis, a seven-hour forecast was run using cycle 46 (the operational version during 1992) of the ECMWF medium-range forecast model and an hourly time series of the accumulated ω since the beginning of the forecast was constructed. An hourly time series of ω was constructed using a centered difference of accumulated ω between an hour before and an hour after the time in question. With hours

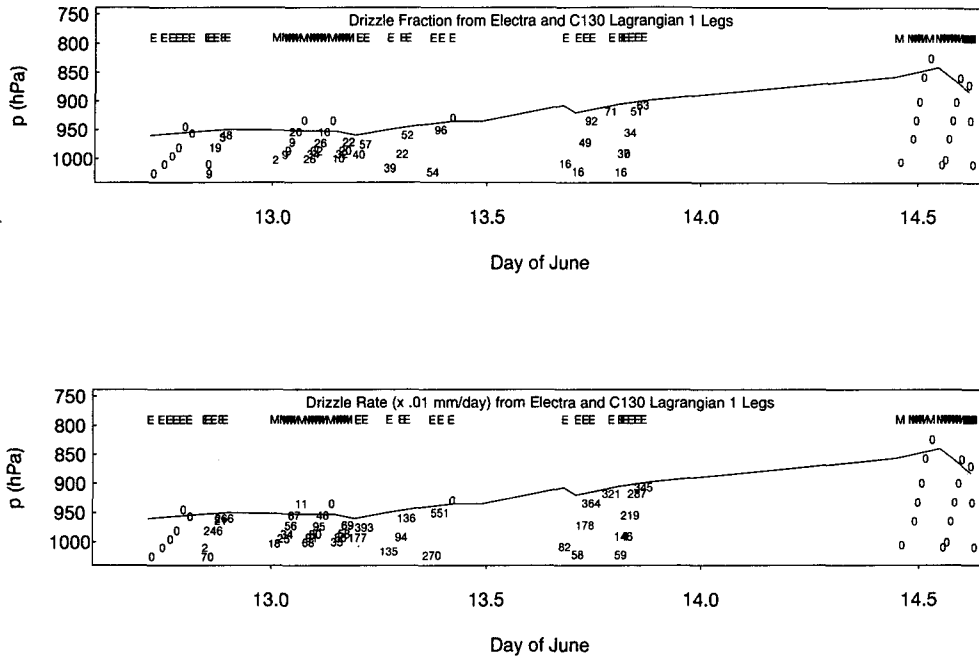


FIG. 6. Drizzle frequency and rain rate for L1. The solid line indicates the inversion base from sounding data. Each number corresponds to one Electra (E) or C130 (M) leg and is plotted at the leg pressure and time. The letter above the leg indicates the data-taking aircraft.

0–7 of the forecast, an ω field for hours 1–6 after each analysis (hour 0) was derived. Figure 8 shows the ECMWF-derived vertical pressure velocity ω_i (>0 for subsidence) at the trade inversion base for L1 and L2.

This was calculated as the ω at the instantaneous trajectory position and observed inversion pressure. The prominent oscillations of ω_i (due to slight dynamical imbalance between the ECMWF initialized winds and

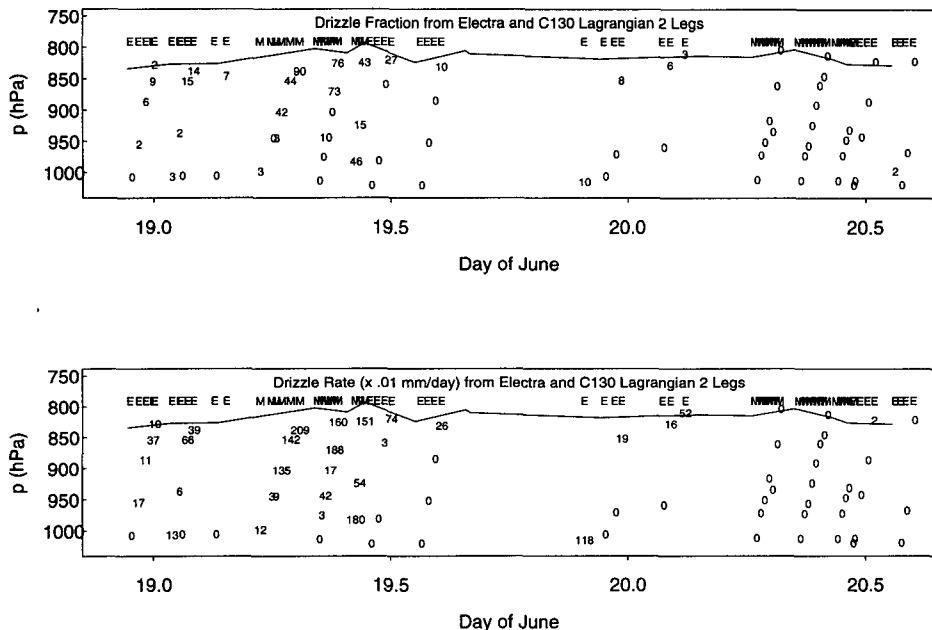


FIG. 7. As in Fig. 6 but for L2.

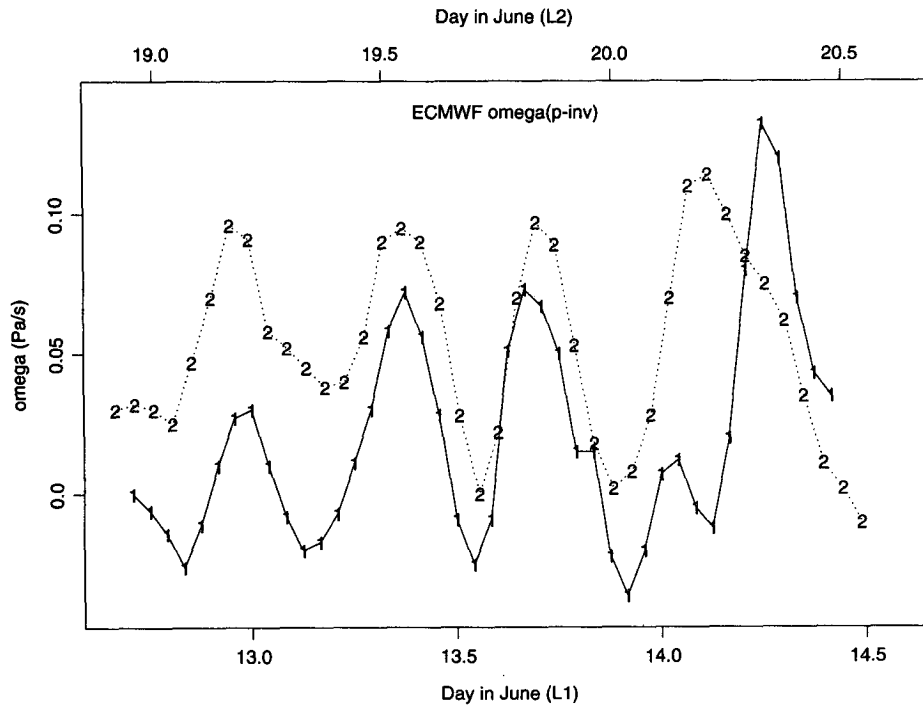


FIG. 8. The ECMWF ω_i at the (changing) inversion pressure for Lagrangians 1–2.

pressures) are not large compared to vertical motions in midlatitude storms but are as large as the typical values of subsidence, 0–0.1 Pa s⁻¹, that we expect to see. Thus, this method can be applied only to much longer averaging timescales—for example, the entire duration of a Lagrangian IOP. We averaged ω_i over

each Lagrangian IOP, found the average rate of change of the inversion pressure dp_i/dt , and estimated the mean entrainment rate $w_e = (\omega_i - dp_i/dt)/\rho_i g$ (Table 2). We estimate the error from three independent uncertainties—a nominal 0.03 Pa s⁻¹ in the mean ω_i due to the large oscillation, a negligible 0.01 Pa s⁻¹ uncer-

TABLE 2. Entrainment rates for the Lagrangians.

Method	Lagrangian number	Decimal day	Mean w_e (cm s ⁻¹)	Mean ω_i (Pa s ⁻¹)	dp/dt (Pa s ⁻¹)
ECMWF	1	12.71–14.41	0.9 ± 0.5	0.03 ± 0.05	0.07
	2	18.91–20.54	0.6 ± 0.3	0.06 ± 0.03	0.00
Budget	1	12.71–14.41	1.0 ± 0.4	0.04 ± 0.04	0.07
	2	18.91–20.54	0.9 ± 0.3	0.09 ± 0.03	0.00
Ozone	1	12.80	0.2	$\langle w'O_3 \rangle$ -0.010	ΔO_3 ppbv 5
	1	13.33	0.9	0.023	-3
	1	13.34	0.8	0.035	-4
	1	13.77	0.3	-0.026	8
	1	Mean	0.6 ± 0.5		
	2	19.12	1.0	-0.192	20
	2	19.52	0.1	0.006	-5
	2	19.63	0.2	-0.011	7
	2	20.02	0.0	-0.007	25
	2	20.13	0.2	-0.048	25
	2	20.60	0.0	-0.007	35
	2	Mean	0.3 ± 0.5		
	Consensus	1	12.71–14.41	0.7 ± 0.3	
2		18.91–20.54	0.6 ± 0.3		

tainty in the 40-hour mean dp_i/dt due to the effect of observed ± 10 -hPa mesoscale variations in p_i , and possible systematic errors in the analyses (which we believe may be present in L1).

We might expect the rapid deepening of the MBL in the second half of L1 to be associated with vertical lifting ($\omega_i < 0$). This is not evident in Fig. 8. Satellite imagery suggested that there was an upper-level subtropical disturbance over the trajectory on the morning of 14 June. This disturbance and any associated low-level convergence was to the east of the trajectory in the ECMWF 0000 UTC analysis. Thus, it is possible that the analysis systematically overestimated ω_i in the latter half of L1. An additional 0.02 Pa s^{-1} has been added to the uncertainty in ω_i to account for this.

The ECMWF ω_i (and hence w_e) should have been more reliable in L2 than in L1 since L2 took place in the heart of the ASTEX triangle, where soundings from the nearby R/V *Oceanus* and all three triangle corners as well as the R/V *Oceanus* were being assimilated into the analyses. Figure 8 shows little systematic trend in ω_i , consistent with the observed steady inversion pressure.

b. MBL water budget

The Lagrangian observation strategy is ideal for budget calculations because horizontal advection into and out of the air column is insignificant. The water budget of the MBL is of particular interest since the only term not directly measured is the entrainment drying. This allows the entrainment rate to be calculated by inferring entrainment drying as a residual.

We assume for simplicity that the horizontal divergence D and the area-averaged horizontal velocity components \bar{u} and \bar{v} are constant with height within the MBL. Consider a scalar with mixing ratio $\xi = \bar{\xi} + \xi'$ and an internal source $S(x, y, p, t)$. Here $\bar{\xi}(x, y, p, t)$ is the horizontal average of ξ over an area large compared to individual turbulent circulations (i.e., 50–100 km on a side for the ASTEX MBL) and $\xi'(x, y, p, t)$ is the local perturbation from this mean. The transport equation is

$$\partial\xi/\partial t + u\partial\xi/\partial x + v\partial\xi/\partial y + \omega\partial\xi/\partial p = S. \quad (2)$$

Invoking the continuity equation $\partial u/\partial x + \partial v/\partial y + \partial\omega/\partial p = 0$ to put (2) into flux form and writing it in terms of means and perturbations, we obtain

$$\begin{aligned} \partial\bar{\xi}/\partial t + \bar{u}\partial\bar{\xi}/\partial x + \bar{v}\partial\bar{\xi}/\partial y \\ + \bar{\omega}\partial\bar{\xi}/\partial p + \partial(\bar{u}'\xi')/\partial x + \partial(\bar{v}'\xi')/\partial y \\ + \partial(\bar{\omega}'\xi')/\partial p = \bar{S}. \end{aligned} \quad (3)$$

Over a large horizontal averaging area the terms $\partial(\bar{u}'\xi')/\partial x$, $\partial(\bar{v}'\xi')/\partial y$ can be neglected. Then $d\bar{\xi}/dt = \partial\bar{\xi}/\partial t + \bar{u}\partial\bar{\xi}/\partial x + \bar{v}\partial\bar{\xi}/\partial y$ is the ‘‘Lagrangian’’ derivative of $\bar{\xi}$ following a moving MBL air col-

umn, which is what we measure in the Lagrangian IOPs. With these simplifications, (3) can be written

$$d\bar{\xi}/dt + \bar{\omega}\partial\bar{\xi}/\partial p + \partial(\bar{\omega}'\xi')/\partial p = \bar{S}. \quad (4)$$

We define the column-averaged ξ_a to be the mass-weighted average of $\bar{\xi}$ over the MBL. A constant horizontal divergence $d\bar{\omega}/dp = D$ does not affect ξ_a , because it squeezes mass out of each part of a vertical column at an equal rate. Thus, ξ_a is affected only by entrainment, by surface fluxes $F_{\xi 0}$ of ξ , and by the internal source averaged over the height of the MBL, S_a . Taking the average of (4) between the surface pressure $p_s(t)$ and the inversion pressure $p_i(t)$, we obtain

$$d\xi_a/dt = g\{F_{\xi 0} + \rho_i w_e(\xi_i^+ - \xi_a)\}/(p_s - p_i) + S_a, \quad (5)$$

where ξ_i^+ is the mean mixing ratio of ξ just above the inversion, ρ_i is the density at the inversion base, and w_e is the entrainment rate of air through the inversion. By using pressure coordinates, we need not make the assumption that ρ is independent of time at all heights, as required in a comparable derivation by Betts (1992).

Applying (5) to the MBL column-averaged total water (vapor + liquid) mixing ratio $q_a(t)$, we obtain

$$dq_a/dt = g\{\rho_i w_e(q_i^+ - q_a) + F_{q 0} - R\}/(p_s - p_i), \quad (6)$$

where $F_{q 0}$ is the upward surface water vapor flux and $-R$ is the surface drizzle flux. This may be solved for w_e :

$$\rho_i w_e\{q_a - q_i^+\} = F_{q 0} - R - (p_s - p_i)(dq_a/dt)/g. \quad (7)$$

All quantities except w_e are known from the soundings and surface fluxes.

The resulting formula (7) was averaged for the length of each Lagrangian IOP to determine the mean value of w_e . The terms in (7) were evaluated as follows.

1) Lagrangian IOP-averaged surface latent heat fluxes (Fig. 3) were $100 \pm 20 \text{ W m}^{-2}$ for both L1 and L2. (Some of the estimated uncertainty is due to the use of bulk formulas, and some due to sampling scatter and lack of data coverage.) Lagrangian IOP-averaged surface drizzle flux was estimated from Fig. 6 to be $1 \pm 0.5 \text{ mm day}^{-1}$ (or $-30 \pm 15 \text{ W m}^{-2}$) for L1, and from Fig. 7 to be $0.1 \pm 0.1 \text{ mm day}^{-1}$ ($-3 \pm 3 \text{ W m}^{-2}$) for L2. Combining the drizzle flux with the latent heat flux and assuming uncorrelated uncertainties, the net surface moisture flux $F_{q 0} - R = 2.8 \pm 1.0 \times 10^{-5} \text{ kg m}^{-2} \text{ s}^{-1}$ ($70 \pm 25 \text{ W m}^{-2}$) for L1 and $4.0 \pm 0.8 \times 10^{-5} \text{ kg m}^{-2} \text{ s}^{-1}$ ($97 \pm 20 \text{ W m}^{-2}$) for L2.

2) Figure 9 shows q_a and q_i^+ for the 17 soundings in each Lagrangian IOP, where q_i^+ was evaluated 30 hPa above the inversion base (shown in Fig. 6 for L1 and Fig. 7 for L2). From this data we estimate that for

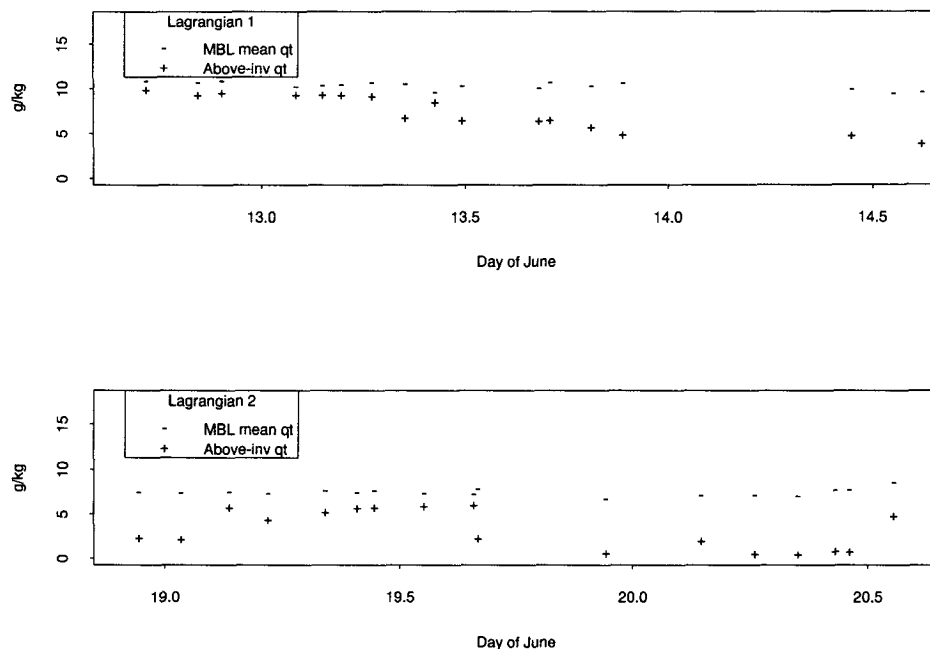


FIG. 9. The mixing ratios q_a and q_i^+ for the 17 soundings in each Lagrangian.

L1 the mean $q_a = 10.1 \pm 0.2 \text{ g kg}^{-1}$, the mean $q_i^+ = 6.9 \pm 0.4 \text{ g kg}^{-1}$, and the mean $(p_s - p_i)(dq_a/dt)/g = -0.7 \pm 0.5 \times 10^{-5} \text{ kg m}^{-2} \text{ s}^{-1}$. Similarly, for L2, the mean $q_a = 7.3 \pm 0.1 \text{ g kg}^{-1}$, the mean $q_i^+ = 3.2 \pm 0.3 \text{ g kg}^{-1}$, and the mean $(p_s - p_i)dq_a/dt = 0.2 \pm 0.5 \times 10^{-5} \text{ kg m}^{-2} \text{ s}^{-1}$. Using these estimates in (7), we conclude (Table 2) that the mean $w_e = 1.0 \pm 0.4 \text{ cm s}^{-1}$ for L1 and $w_e = 0.9 \pm 0.3 \text{ cm s}^{-1}$ for L2.

c. Electra fast ozone flux-jump method

Since ozone has only weak sources and sinks at the inversion, the entrainment rate can be estimated in terms of its below-inversion flux and across-inversion jump (Kawa and Pearson 1989):

$$w_e = \langle w'O_3' \rangle_{I-} / \Delta O_3. \quad (8)$$

We used an eddy correlation method based on the fast ozone measurements on the highest below-inversion legs of all the Electra stacks during the two Lagrangian IOPs to determine below-inversion ozone fluxes. The 60-km leg time series were detrended, tapered to reduce end effects, and high-pass filtered using a cutoff wavelength equal to 100 times the integral length scale based on the covariance of w . The cutoff wavelength was 10–12 km for L1 and 20–30 km for L2. It is extremely difficult to assess the accuracy of the filtered fluxes; our impression is that they can be trusted only to $O(\pm 50\%)$ at best. Each ozone jump across the inversion was estimated from a porpoising leg. The measured ΔO_3 varied greatly (-5 to 25 ppbv) during both Lagrangian IOPs. In Table 2, we present w_e only for stacks for

which ΔO_3 was both consistent and at least 3 ppbv in absolute value. A typical measurement uncertainty for ΔO_3 is 1–2 ppbv. We assign a nominal uncertainty of $\pm 0.5 \text{ cm s}^{-1}$ to ozone-derived w_e .

d. Synthesis

All three methods provide consistent albeit quite uncertain estimates of w_e . For both Lagrangian IOPs, the budget calculation gives high w_e 's. This may reflect a systematic overestimate of latent heat fluxes or underestimate of drizzle fluxes. For L1, the ozone method suffers from rather small and variable ΔO_3 for L1, but the mean of the four ozone-derived entrainment rates (0.6 cm s^{-1}) is quite plausible. As mentioned earlier, we anticipate that the ECMWF-derived ω_i (and hence w_e) is probably high for L1. A best-guess L1 mean $w_e = 0.7 \text{ cm s}^{-1}$ is consistent with all three methods. This implies a mean $\omega_i = 0.01 \text{ Pa s}^{-1}$ during L1. In Part I, we found that the time evolution of O_3 and q_v above the inversion suggested initially strong subsidence, consistent with a horizontal divergence in the range 4 – $6 \times 10^{-6} \text{ s}^{-1}$ for the first 16 hours, changing to no subsidence and then weak ascent thereafter. A best-guess horizontal divergence $D(t) = 5 \times 10^{-6} \text{ s}^{-1}$ between the surface and the marine inversion before day 13.4, decreasing linearly to $-1 \times 10^{-6} \text{ s}^{-1}$ by day 13.75 and constant thereafter, is consistent with all available information.

For L2, much of the entrainment may have been associated with vigorous patchy cumuli that the Electra might or might not intersect on a given flight leg; thus,

the ozone estimates are quite scattered. The budget method has less random uncertainty than in L1 since little precipitation was encountered but could have systematic errors due to misestimation of surface latent heat fluxes. The ECMWF ω_i seems to be a good compromise for L2; a best-guess L2 mean w_e of 0.6 cm s^{-1} is within the error bounds of all three methods. The constant inversion height suggests that mean vertical motion was nearly constant throughout L2, with a mean horizontal divergence of $3 \times 10^{-6} \text{ s}^{-1}$ between the surface and the marine inversion throughout the period. While the increase in cloud and slight increase in inversion depth around day 19.4 might be associated with weakened subsidence, it may also reflect the entrainment of comparatively moist air, which would be conducive to more stratocumulus formation and possibly to enhanced entrainment by these stratocumulus.

4. Some MBL timescales

It is often convenient (e.g., for looking at chemical transport or in constructing parameterizations for boundary layer thermodynamic structure) to have estimates of internal circulation or mixing timescales within a boundary layer. During ASTEX, visual and millimeter-wavelength radar observations, in addition to aircraft measurements of the kind discussed here, indicate that the MBL was generally “cumulus-coupled,” that is, that patches of cumulus cloud rise out of a moist subcloud layer through a conditionally unstable layer and detrain into a thin, often patchy stratocumulus layer (Albrecht et al. 1995). For a cumulus-coupled MBL there are internal circulation timescales associated with the subcloud layer and with the cumulus–stratocumulus layer. An important external timescale is the “dilution” timescale in which a sizable fraction of the air is diverged laterally out of the MBL air column and replaced by air entrained from above. During L2, the thermodynamic structure was typical of a deep cumulus-coupled MBL and varied little from sounding to sounding. We apply techniques based on the structure of a representative sounding supplemented by knowledge of surface fluxes to estimate these timescales, using concepts from Bretherton (1993), Albrecht et al. (1979), Betts (1975), and others. As a corollary of these calculations, we also estimate the areally averaged vertical mass flux vented out of the subcloud layer by cumulus clouds.

In an air column advected toward warmer water, the subcloud mixed layer will usually be turbulently mixed and derive much of its energy from upward surface buoyancy fluxes. Shear-driven mixing in the subcloud mixed layer may often be important as well. A velocity scale for a mixed layer of depth z_B driven by surface buoyancy fluxes $(\overline{w'b'})_0$ is $w^* = \{(\overline{w'b'})_0 z_B\}^{1/3}$. The associated circulation timescale for the subcloud mixed layer is

$$\tau_M = z_B/w^*. \quad (9)$$

The dilution timescale due to entrainment into an MBL of depth z_I due to entrainment and horizontal divergence is

$$\tau_E = z_I/w_e \quad (= D^{-1} \text{ for a steady-state inversion height}). \quad (10)$$

The circulation timescale for the cumulus–stratocumulus layer is estimated by assuming that after air enters a cumulus cloud, it rises rapidly, detraining into the stratocumulus layer. After turbulently mixing with above-inversion air at both the cumulus and stratocumulus cloud tops, it slowly subsides from the MBL top back to the top subcloud mixed layer, where it is entrained, moistened, and warmed by surface fluxes, and is rapidly primed to undergo another cycle. The slow subsidence takes far longer than the other stages of the circulation.

We can estimate the subsidence time from the following assumptions.

1) The upward latent heat flux at the cumulus cloud base is the same as at the surface latent heat flux $F_L = \rho_s L \langle w'q'_v \rangle$. This neglects moisture storage due to time rate of change of mixing ratio in the subcloud layer. A $1 \text{ g kg}^{-1} \text{ day}^{-1}$ rate of change in mixing ratio over a 500-m-thick subcloud layer would require a latent heat flux divergence of only 17 W m^{-2} ; the observed change in subcloud layer mixing ratio over L2 was nearly zero and certainly much smaller than $1 \text{ g kg}^{-1} \text{ day}^{-1}$.

2) The small inversion (and moisture jump) at the entrainment interface at the top of the subcloud layer is often called the transition layer (a typical example is the 950–960-hPa level in the first sounding of L2, shown in Fig. 20 of Part I). We assume that the mixing ratio difference across the transition layer is representative of the cloud–environment mixing ratio difference Δq_c at cloud base.

Then the cumulus cloud base mass flux needed to support the observed latent heat flux by exporting air from the subcloud layer and entraining an equal amount of air from above the transition layer into the subcloud layer is

$$M_c = F_L / (L \Delta q_c). \quad (11)$$

The subsidence timescale

$$\tau_c = p_c / (\omega_c + \bar{\omega}) \quad (12)$$

for a cumulus layer of pressure depth p_c is due to a combination of compensating subsidence with pressure velocity $\omega_c = gM_c$ (vertical velocity $w_c = -M_c/\rho = -\omega_c/\rho g$) and mean subsidence with pressure velocity $\bar{\omega}$.

Last, we can estimate the areally averaged cumulus updraft fraction

$$\sigma_c = M_c / (\rho_c w_U) \quad (13)$$

in the cumulus layer by assuming that the updraft velocity w_U in clouds that penetrate through the transition layer is driven by the conditional available potential energy in a typical sounding; for example, $w_U = 0.3(\text{CAPE})^{1/2}$. The coefficient 0.3 is chosen arbitrarily to reflect the reduction of the updraft strength from its maximum possible value by entrainment-driven evaporative cooling and by pressure forces. Here, ρ_c is a characteristic density in the cumulus layer.

We now apply these estimates to a typical sounding from L2 (e.g., Fig. 20 of Part I), which has a 110-hPa-thick cumulus layer extending from 950 to 840 hPa, a CAPE of 45 J kg^{-1} , and $w_U = 2 \text{ m s}^{-1}$. From Figs. 19 and 20 of Part I, the subcloud layer had mixing ratios of 9 g kg^{-1} , and the cumulus layer had mixing ratios of 7 g kg^{-1} at the beginning of L2 and 6 g kg^{-1} toward the end. Using a representative $\Delta q_c = 2.5 \text{ g kg}^{-1}$ and latent heat flux $F_L = 125 \text{ W m}^{-2}$, we find a cumulus mass flux $M_c = 0.02 \text{ kg m}^{-2} \text{ s}^{-1}$ and a compensating subsidence rate of $\omega_c = 0.2 \text{ Pa s}^{-1}$. From the results of section 3, a reasonable average $\bar{\omega}$ over the cumulus layer was 0.04 Pa s^{-1} . We deduce from (9) that the subcloud layer circulation timescale that the cumulus-stratocumulus-layer circulation time was $\tau_c = 0.5$ day and that the updraft fraction was $\sigma_c = 0.01$. This updraft fraction should be thought of as including vigorous updrafts within cumuli that extend through the entire depth of the cumulus cloud layer. The areal coverage of cloud at a given level, which also includes detrained or "passive" cloud, will in general be much larger.

From the above latent heat flux and a typical sensible heat flux $F_S = 5 \text{ W m}^{-2}$ for L2, the surface buoyancy flux $(w'b')_0 = 4 \times 10^{-4} \text{ m}^2 \text{ s}^{-3}$. For a subcloud layer of depth $z_i = 600 \text{ m}$, we find that the characteristic eddy vertical velocity in the subcloud layer was $w^* = 0.6 \text{ m s}^{-1}$ and that the subcloud mixed layer timescale was $\tau_M = 1000 \text{ s}$, which is much shorter than τ_c .

Since there was little systematic change in inversion height during L2, the dilution timescale can be found from the horizontal divergence $D = 3 \times 10^{-6} \text{ s}^{-1}$ and (7) to be $\tau_E = 4$ days. This is much longer than τ_c , so rapid variations in above-inversion properties have little impact on the MBL itself, as seen for instance in the ozone profiles for L2 shown in Part I.

5. Conclusions

In conjunction with Part I, we have endeavored to provide an overview of the ASTEX Lagrangian IOPs. In Part II we have concentrated on obtaining horizontal averages of SST, surface fluxes, cloudiness, drizzle fluxes, and entrainment rate. The density of aircraft data and the Lagrangian strategy allowed these to be measured with unprecedented confidence over a period

long enough to examine the water budget of the MBL. Three techniques of measuring entrainment were compared; large uncertainties exist in all of them but they are all consistent with a $0.6 \pm 0.5 \text{ cm s}^{-1}$ average entrainment rate for both Lagrangian IOPs.

The most important leg-averaged quantities not analyzed in this study are the radiative and turbulent fluxes. Patchy cirrus overlying the MBL during parts of L2 may have increased downwelling longwave radiation and decreased downwelling shortwave radiation onto the top of the MBL compared to a clear sky. We intend to carry out a detailed analysis of the broadband radiative fluxes from the Lagrangian IOPs in a forthcoming paper. The turbulent fluxes may prove difficult to reliably analyze, because the cumulus clouds rising into the stratus led to substantial spatial inhomogeneity throughout the cloud layer.

Because of their detail and consistency, the ASTEX Lagrangian datasets will provide a superb test case for MBL parameterizations and models in the transitional region between stratocumulus and cumulus. The Lagrangian strategy should be further used as we try to better understand the complex feedbacks that produce MBL cloudiness.

Acknowledgments. This work was supported by ONR Grants N00014-90-J-1136 and N00014-90-F0037 [under Interagency Agreement (IA) 89-12 and NOAA Grant NA37RJ0203]. Dr. Alan Betts helped clarify the water budget analysis, and Dr. Barry Huebert of the University of Hawaii provided inspiration at many times. C130 data were provided by Dr. Doug Johnson of the UKMRF. Matt Wyant and Steven Klein provided insightful criticisms that improved this paper.

REFERENCES

- Albrecht, B. A., A. K. Betts, W. Schubert, and S. K. Cox, 1979: A model of the thermodynamic structure of the trade-wind boundary layer. Part I: Theoretical formulation and sensitivity tests. *J. Atmos. Sci.*, **36**, 73–89.
- , C. S. Bretherton, and D. Johnson, 1995: The Atlantic Stratocumulus Transition Experiment (ASTEX). *Bull. Amer. Meteor. Soc.*, **76**, 889–904.
- Beard, K. V., 1976: Terminal velocity and shape of cloud and precipitation drops aloft. *J. Atmos. Sci.*, **33**, 851–864.
- Betts, A. K., 1975: Parameteric interpretation of trade-wind cumulus budget studies. *J. Atmos. Sci.*, **32**, 1934–1945.
- , 1992: FIFE atmospheric boundary layer methods. *J. Geophys. Res.*, **97**, 18 523–18 531.
- Bretherton, C. S., 1993: Understanding Albrecht's model of trade cumulus cloud fields. *J. Atmos. Sci.*, **50**, 2264–2283.
- Garratt, 1977: Review of drag coefficients over oceans and continents. *Mon. Wea. Rev.*, **105**, 915–929.
- Kawa, S. R., and R. Pearson Jr., 1989: An observational study of stratocumulus entrainment and thermodynamics. *J. Atmos. Sci.*, **46**, 2649–2661.
- Stull, R. B., 1988: *An Introduction to Boundary Layer Meteorology*. Kluwer, 666 pp.